Proc. IEEE Computer Vision and Pattern Recognition (CVPR) 2017

Multiple-Scattering Microphysics Tomography

Aviad Levis, Yoav Y. Schechner
Viterbi Faculty of Electrical Engineering
Technion - Israel Institute of Technology
Haifa, Israel
aviad.levis@gmail.com ; yoav@ee.technion.ac.il

Anthony B. Davis
Jet Propulsion Laboratory
California Institute of Technology
Pasadena, CA, USA
Anthony.B.Davis@jpl.nasa.gov

Abstract

Scattering effects in images, including those related to haze, fog and appearance of clouds, are fundamentally dictated by microphysical characteristics of the scatterers. This work defines and derives recovery of these characteristics, in a three-dimensional (3D) heterogeneous medium. Recovery is based on a novel tomography approach. Multi-view (multi-angular) and multi-spectral data are linked to the underlying microphysics using 3D radiative transfer, accounting for multiple-scattering. Despite the nonlinearity of the tomography model, inversion is enabled using a few approximations that we describe. As a case study, we focus on passive remote sensing of the atmosphere, where scatterer retrieval can benefit modeling and forecasting of weather, climate and pollution.

1. Introduction

Until recently, 3D inverse problems in computer vision tended to use simple forward models, such as blur (defocus, motion), reflection (photometric stereo), and dehazing [33, 42] based on single-scattering [5,48,49]. Other imaging communities use different simplified models. Specifically, tomography in medical imaging and many other applications is based on linear models [19,21,38,51]. Scattering is often considered a nuisance, thus attempts are made to counter or ignore it. In contrast, in atmospheric and hydrologic remote sensing, multiple scattering is a major signal source, and the dominant light source (Sun) is uncontrolled. Multiple-scattering models [46] are used resulting in a nonlinear inversion. However, the model of the medium degenerates to a *plane parallel* structure [30,36,39]: scatterers vary essentially only in the 1D altitude [12,34].

With increasing computing power, previously intractable problems may now be considered. Advances are made in multiple reflections, non-line-of-sight imaging [4,29,47] and multiple scattering [17,18,27,31,35]. In this line, this work fits a 3D forward model involving arbitrary orders of scattering, multiple viewpoints and spectral bands. We apply this approach to 3D atmospheric remote sensing, however, it could also find use in other fields such as computer graphics, bio-medical imaging and material science.

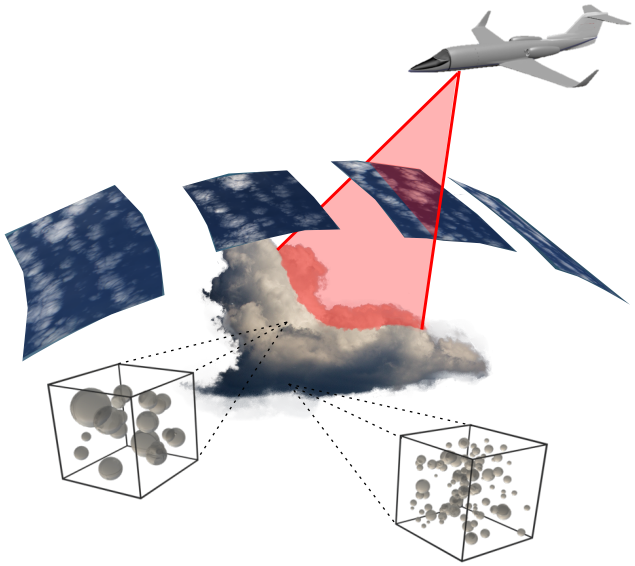

Figure 1. An instrument acquires multi-view images of a volumetric scattering medium. In each voxel, the scatterers have a different size-distribution. The microphysical parameters of the size-distribution, coupled with Mie theory, determine a voxel's effective scattering characteristics, therefore affecting the acquired images. Using these multi-view multi-spectral measurements we recover spatial variations in the size-distribution parameters.

Prior art has shown 3D scattering tomography of optical parameters [17,18], however, it does not retrieve the physical properties of the scattering particles. The particles are the crux, scientifically. Their *microphysical* parameters directly relate to physical, chemical and even biological processes in the medium. For example, in the atmosphere, microphysical properties of particles dictate pollution, cloud formation and climate changes [9,45].

This paper seeks to recover these fundamental parame-

ters, in 3D, using multiview multiband images (Fig. 1). To achieve this, we generalize the mathematical approach of scattering tomography in several ways. First, we generalize the forward and inverse models, so that they explicitly and directly relate to the microphysical parameters, hence retrieving them in 3D. Second, we generalize the 3D forward and inverse models to include multi-spectral data, to enhance sensitivity to the microphysics.

We apply our approach to remote-sensing of clouds, for which the scatterer material is known, retrieving size-distribution parameters only. We conclude with a possible *road-map*, to include retrieval of an unknown refractive index, e.g. for remote sensing and discrimination of smoke and dust plumes.

2. Background

This section describes a microphysical parameterization of a scattering medium and the connection between microphysics and the image formation (forward) model .

2.1. Scatterer Microphysics

Microphysical properties of scatterers are parameterized by a vector $\boldsymbol{\nu}$. For spherical scatterers, a common parameterization [22] expresses the number density distribution, $n(r|\boldsymbol{\nu})$, of particles of radius r (Fig. 1). Let $N, r_{\mathrm{e}}, v_{\mathrm{e}}$ be the total number concentration, effective radius and the dimensional-less variance defined [22] as

$$N = \int n(r|\boldsymbol{\nu})\mathrm{d}r, \quad r_{\mathrm{e}} = \frac{\int(\pi r^2) r n(r|\boldsymbol{\nu})\mathrm{d}r}{\int(\pi r^2) n(r|\boldsymbol{\nu})\mathrm{d}r}, \tag{1}$$

$$v_{\mathrm{e}} = \frac{\int (r-r_{\mathrm{e}})^2 (\pi r^2) n(r|\boldsymbol{\nu})\mathrm{d}r}{r_{\mathrm{e}}^2 \int(\pi r^2) n(r|\boldsymbol{\nu})\mathrm{d}r}. \tag{2}$$

Assume the scattering particles are of the same type, having a *known* complex refractive index m (Sec. 9 discusses retrieval of m). Thus, $\boldsymbol{\nu}=[N, r_{\mathrm{e}}, v_{\mathrm{e}}]$. Cloud water droplets have good empirical agreement [22] with the *Gamma*-distribution (Fig. 2):

$$n(r|\boldsymbol{\nu}) = NC r^{(v_{\mathrm{e}}^{-1}-3)} \exp[-r/(r_{\mathrm{e}} v_{\mathrm{e}})], \tag{3}$$

where $C=(r_{\mathrm{e}} v_{\mathrm{e}})^{(2-v_{\mathrm{e}}^{-1})}/\Gamma(v_{\mathrm{e}}^{-1}-2)$ is a normalization constant. An important bulk characteristic is the *mass content* defined as

$$\mathbb{M} = \frac{4}{3}\pi\rho \int_r r^3 n(r|\boldsymbol{\nu})\mathrm{d}r, \tag{4}$$

where ρ is the particle density. For water $\rho_{\mathrm{w}}=1\,\mathrm{g/cm^3}$ and $\mathbb{M}_{\mathrm{w}}$ is referred to as *liquid water content*.

2.2. Single Scattering

Consider an incident planewave of wavelength λ scattered from a spherical particle of radius r. Scattering of radiant intensity is described in terms of an interaction cross-section [3] (extinction for a distribution of particles) and angular scattering function. The scattering angle cosine, μ, is defined in 3D as a product of unit direction vectors (Fig. 3) $\boldsymbol{\omega}$ and $\boldsymbol{\omega}'$

$$\mu = \cos\theta = \boldsymbol{\omega}\cdot\boldsymbol{\omega}'. \tag{5}$$

Define the size-parameter as

$$d = 2\pi r/\lambda. \tag{6}$$

The *Rayleigh* model describes light scattering by particles much smaller than wavelength, where $d\to 0$. For molecules the interaction cross-section,[1] σ^{Rayl}, is approximately proportional to λ^{-4}. Let N^{Rayl} denote the number density. The

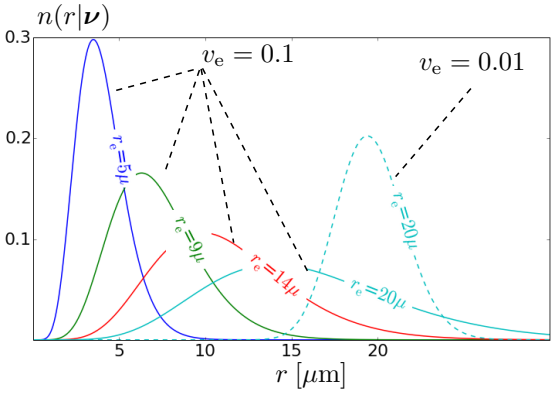

Figure 2. Normalized (N=1) *Gamma*-distribution. A decrease in effective variance shifts the peak toward larger values as well as decreasing the overall width of the distribution.

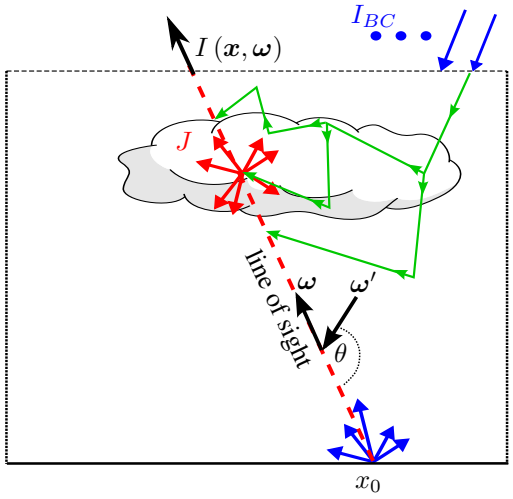

Figure 3. Light scatters in the medium, generally multiple times, creating a scatter field J (Eq. 20). Integration yields the light field I (Eq. 19). The angle between the two unit direction vectors $\boldsymbol{\omega}$, $\boldsymbol{\omega}'$ is θ. The boundary radiation is I_{BC} and x_0 is the intersection point of the line-of-sight and the domain boundary.

[1] For air, a mixture of molecules, the cross-section is an average quantity.

molecular extinction [11] is

$$\beta_\lambda^{\text{Rayl}} = \sigma_\lambda^{\text{Rayl}} N^{\text{Rayl}}. \tag{7}$$

Expressing diversion of radiance from $\boldsymbol{\omega}'$ to $\boldsymbol{\omega}$, the angular scattering function is

$$f_\lambda^{\text{Rayl}}(\mu) = \sigma_\lambda^{\text{Rayl}} N^{\text{Rayl}} \frac{3}{16\pi}(1+\mu^2). \tag{8}$$

Rayleigh scattering by molecules is often compounded by scattering from large particles. For spherical particles of size comparable to λ, the Mie model applies. Mie theory provides a link between microphysical and optical properties of a medium.[2] In the following, we introduce the equations necessary to describe the interaction cross-section, $\sigma_\lambda^{\text{Mie}}$, and intensity scattering function f_λ^{Mie}. For a comprehensive analysis we refer the reader to [20], where the notations used in this section are taken from.[3]

Denote spherical *Bessel* and *Hankel Functions* [1] of the *First Kind* as $j_l(q)$ and $h_l(q)$ respectively. Here $l \in \mathbb{N}^+$, $q \in \mathbb{C}$. The *Ricatti-Bessel* functions are

$$\Psi_l(q) = q j_l(q),\ \xi_l(q) = q h_l^{(1)}(q). \tag{9}$$

Their respective derivatives are

$$\Psi_l'(q) = \frac{d}{dq}\Psi_l(q),\ \xi_l'(q) = \frac{d}{dq}\xi_l(q). \tag{10}$$

For radius r and complex refractive index m, Mie series coefficients are

$$a_l^\lambda(r|m) = \frac{\Psi_l(d)\Psi_l'(md) - m\Psi_l(md)\Psi_l'(d)}{\xi_l(d)\Psi_l'(md) - m\Psi_l(md)\xi_l'(d)}, \tag{11}$$

$$b_l^\lambda(r|m) = \frac{m\Psi_l(d)\Psi_l'(md) - \Psi_l(md)\Psi_l'(d)}{m\xi_l(d)\Psi_l'(md) - \Psi_l(md)\xi_l'(d)}, \tag{12}$$

where d is defined in Eq. (6). Let P_l^1 denote the *Associated Legendre Polynomial* [1] of first order and degree l. Define the angular functions

$$\pi_l(\mu) = \frac{P_l^1(\mu)}{\sin\theta}, \quad \tau_l(\mu) = \frac{dP_l^1(\mu)}{d\theta}. \tag{13}$$

Using (11,12,13), define the amplitude scattering functions

$$S_1^\lambda(\mu, r|m) = \sum_{l=1}^{\infty} \frac{2l+1}{l(l+1)} \left[a_l^\lambda \pi_l(\mu) + b_l^\lambda \tau_l(\mu)\right], \tag{14}$$

$$S_2^\lambda(\mu, r|m) = \sum_{l=1}^{\infty} \frac{2l+1}{l(l+1)} \left[a_l^\lambda \tau_l(\mu) + b_l^\lambda \pi_l(\mu)\right]. \tag{15}$$

With these definitions, the Mie intensity scattering function (Fig. 4) and cross-section are given respectively by

$$f_\lambda^{\text{Mie}}(\mu, r|m) = \frac{\lambda^2}{8\pi^2}\left[\left|S_1^\lambda(\mu, r|m)\right|^2 + \left|S_2^\lambda(\mu, r|m)\right|^2\right], \tag{16}$$

$$\sigma_\lambda^{\text{Mie}}(r|m) = \frac{\lambda^2}{2\pi}\sum_{l=1}^{\infty}(2l+1)\Re\left\{a_l^\lambda(r|m) + b_l^\lambda(r|m)\right\}, \tag{17}$$

[2] Accurate for scatterers which are $>\lambda$ apart [7].

[3] Notations slightly differ from those older texts such as [7].

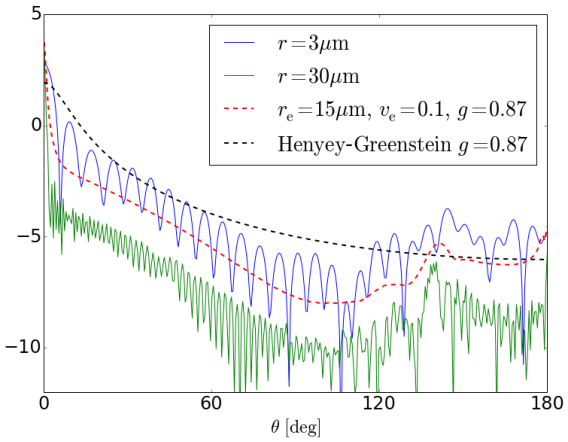

Figure 4. Logarithm of $f_\lambda^{\text{Mie}}(\mu, r|m)$, normalized over θ, for λ=660 nm. [Green, Blue] Single sphere Mie scattering. [Red] Mie scattering by Gamma-distributed spheres. The size integration smoothes-out high-frequency oscillations. [Black] A Henyey-Greenstein function does not express the complexity of Mie scattering.

where $\Re$ denotes the real part.

2.3. Multiple Scattering: Radiative Transfer

In highly scattering media, a diffusion model for radiation scattering is applicable [6,40,41]. To avoid restriction on scattering order, radiative transfer equations describe transport of monochromatic radiation. Transmittance between points $\boldsymbol{x}_1, \boldsymbol{x}_2$ is given by

$$T_\lambda(\boldsymbol{x}_1, \boldsymbol{x}_2) = \exp\left[-\int_{\boldsymbol{x}_1}^{\boldsymbol{x}_2} \beta_\lambda(\boldsymbol{s})\mathrm{d}\boldsymbol{s}\right]. \tag{18}$$

Here $\beta_\lambda(\boldsymbol{s})$ is the extinction coefficient at $\boldsymbol{s}$, a running point on the segment between $\boldsymbol{x}_1$ and $\boldsymbol{x}_2$. The extinction coefficient is comprised of molecular and particle extinction (Eqs. 7,17).

Define $\boldsymbol{x}_0$ as the intersection of the boundary with a ray originating at point $\boldsymbol{x}$ in direction $-\boldsymbol{\omega}$ (Fig. 3). Let $I_\lambda^{\text{BC}}(\boldsymbol{x}_0, \boldsymbol{\omega})$ denote boundary radiation at $\boldsymbol{x}_0, \boldsymbol{\omega}$. The unpolarized[4] non-emissive forward model of radiative transfer can be expressed by the following recursive equations, per wavelength λ. They couple the radiance field I_λ to an in-scatter field J_λ [8]

$$I_\lambda(\boldsymbol{x}, \boldsymbol{\omega}) = I_\lambda^{\text{BC}}(\boldsymbol{x}_0, \boldsymbol{\omega}) T_\lambda(\boldsymbol{x}, \boldsymbol{x}_0) + \int_{\boldsymbol{x}}^{\boldsymbol{x}_0} J_\lambda(\boldsymbol{x}', \boldsymbol{\omega}) T_\lambda(\boldsymbol{x}, \boldsymbol{x}')\,\mathrm{d}\boldsymbol{x}', \tag{19}$$

$$J_\lambda(\boldsymbol{x}, \boldsymbol{\omega}) = \int_{4\pi} f_\lambda(\boldsymbol{x}, \boldsymbol{\omega}\cdot\boldsymbol{\omega}')\, I_\lambda(\boldsymbol{x}, \boldsymbol{\omega}')\,\mathrm{d}\boldsymbol{\omega}'. \tag{20}$$

[4] For unpolarized sensors and source, polarized radiative transfer typically affects results by $\lesssim$1% [23].

In (20), $f_\lambda\left(\boldsymbol{x},\boldsymbol{\omega}\cdot\boldsymbol{\omega}'\right)$ is the effective scattering function at $\boldsymbol{x}$ which is comprised of both Rayleigh and Mie scattering (Eq. 8,16).

3. Spectral-band Integration

Equations (19,20) should be spectrally integrated in a wavelength band Λ. This integration weights the illumination spectrum and sensor sensitivity at $\lambda\in\Lambda$. Passive imaging uses solar illumination, having approximately the spectrum $B(\lambda)$ of a blackbody at temperature $5800°\mathrm{K}$. For unit sensor sensitivity within Λ, and knowing $I_\lambda(\boldsymbol{x},\boldsymbol{\omega})$ for a unitary boundary illumination, we have

$$I_\Lambda(\boldsymbol{x},\boldsymbol{\omega}) = \int\limits_{\lambda\in\Lambda} I_\lambda(\boldsymbol{x},\boldsymbol{\omega})B(\lambda)\mathrm{d}\lambda, \tag{21}$$

with analogous expressions for $J_\Lambda(\boldsymbol{x},\boldsymbol{\omega})$. Simulated spectral integration requires multiple renderings of (19) within any spectral band. The numerical complexity is thus increased. This increase is exacerbated when solving an inverse problem. We therefore use an approximation which is commonly used in remote sensing as well as computer vision models. It is valid if wavelength dependencies within a spectral band are weak. This condition is met when narrow bands are considered, in the absence of molecular absorption.

Using Eqs. (16,17), define spectrally-averaged Mie optical quantities

$$\sigma_\Lambda^{\mathrm{Mie}}(r|m) = \frac{1}{B_\Lambda^{\mathrm{tot}}}\int\limits_{\lambda\in\Lambda} B(\lambda)\sigma_\lambda^{\mathrm{Mie}}(r|m)\mathrm{d}\lambda, \tag{22}$$

$$f_\Lambda^{\mathrm{Mie}}(\mu,r|m) = \frac{1}{B_\Lambda^{\mathrm{tot}}}\int\limits_{\lambda\in\Lambda} B(\lambda)f_\lambda^{\mathrm{Mie}}(\mu,r|m)\mathrm{d}\lambda, \tag{23}$$

where B_Λ^{tot} is the total spectral radiance in Λ. Define

$$\beta_\Lambda(\boldsymbol{\nu}) = \int n(r|\boldsymbol{\nu})\sigma_\Lambda^{\mathrm{Mie}}(r|m)\mathrm{d}r, \tag{24}$$

$$f_\Lambda(\mu|\boldsymbol{\nu}) = \int n(r|\boldsymbol{\nu})f_\Lambda^{\mathrm{Mie}}(\mu,r|m)\mathrm{d}r, \tag{25}$$

$$T_\Lambda\left(\boldsymbol{x}_1,\boldsymbol{x}_2\right) = \exp\left[-\int_{\boldsymbol{x}_1}^{\boldsymbol{x}_2}\beta_\Lambda(\boldsymbol{s})\mathrm{d}\boldsymbol{s}\right]. \tag{26}$$

An *approximate* band-integrated radiative transfer is given by

$$\bar{I}_\Lambda\left(\boldsymbol{x},\boldsymbol{\omega}\right) = I_\Lambda^{\mathrm{BC}}(\boldsymbol{x}_0,\boldsymbol{\omega})T_\Lambda\left(\boldsymbol{x},\boldsymbol{x}_0\right) + \int\limits_{\boldsymbol{x}}^{\boldsymbol{x}_0}\bar{J}_\Lambda(\boldsymbol{x}',\boldsymbol{\omega})T_\Lambda\left(\boldsymbol{x},\boldsymbol{x}'\right)\mathrm{d}\boldsymbol{x}', \tag{27}$$

$$\bar{J}_\Lambda\left(\boldsymbol{x},\boldsymbol{\omega}\right) = \int\limits_{4\pi} f_\Lambda\left(\boldsymbol{x},\boldsymbol{\omega}\cdot\boldsymbol{\omega}'\right)\bar{I}_\Lambda\left(\boldsymbol{x},\boldsymbol{\omega}'\right)\mathrm{d}\boldsymbol{\omega}'. \tag{28}$$

Figure 5. Two test cases, optically thick and thinner cumulus clouds, from an LES-generated cloud field. Rendered at $\Lambda{=}660{\pm}20\,\mathrm{nm}$ using Eq. (21). The clouds have maximum vertical optical depth of $\sim$20 and $\sim$10.

The approximation $\bar{I}_\Lambda$ is *fast* to compute. Computing $\bar{I}_\Lambda$ requires one call to a radiative transfer numerical solver. In contrast, (21) requires multiple calls to a radiative transfer numerical solver (one per λ). Let N_{spectral} denote the number of spectral bands measured. To quantify the approximation error we define

$$e = (1/N_{\mathrm{spectral}})\sum_\Lambda \|\mathbf{MI}_\Lambda - \mathbf{M}\bar{\mathbf{I}}_\Lambda\|_1/\|\mathbf{MI}_\Lambda\|_1. \tag{29}$$

For clouds, this approximation is highly accurate. We demonstrate the approximation (27,28) by comparing renderings of a *Large Eddy Simulator* [37] (LES) cloud field (Fig. 5). The bands $\Lambda{=}\left\{445,470,550,660,865,935\right\}{\pm}20\,\mathrm{nm}$ yield an error of $e_\Lambda{<}0.1\%$.

4. Recovery: Bias and Complexity

Inversion seeks recovery of a scatterer distribution, while a forward model (rendering) is a radiative transfer model. Rendering (26,27,28) depends on the voxel-dependent function $f_\Lambda(\boldsymbol{\omega}\cdot\boldsymbol{\omega}')$ and scalar β_Λ both of which depend on Λ. The function f_Λ is expressed by at least two other wavelength-dependent parameters: single scattering albedo ϖ_Λ and scattering anisotropy g_Λ (first order angular moment of μ). A widely-used model, parameterized by g_Λ, is the *Henyey-Greenstein* model [17,18,24,27], however, it fails to express the complexity of Mie scattering (Fig. 4).

Parameterizing the scattering function using ad-hoc phenomenological parameters $(\varpi_\Lambda, g_\Lambda)$ may bias the recovery. Bias can be reduced using higher order angular terms [16], resulting in a vector of parameters denoted $\mathbf{g}_\Lambda$. Overall, the vector $[\beta_\Lambda,\varpi_\Lambda,\mathbf{g}_\Lambda]$ has N_{params} elements. For N_{voxels} voxels, the forward model (26,27,28) apparently depends on $N_{\mathrm{voxels}}N_{\mathrm{spectral}}N_{\mathrm{params}}$ distinct values. Hence, tomography that relies on forward model (26,27,28) is a problem whose dimensionality scales as $\mathcal{O}(N_{\mathrm{voxels}}N_{\mathrm{spectral}}N_{\mathrm{params}})$. This is inefficient, because the phenomenological parameters are *not* independent across wavelengths. All are derived from a few *microphysical* properties of the scatterers. The microphysical properties are *wavelength-independent* (with the exception of refractive index). Moreover, ignoring the inherent common

denominator of all channels (microphysics), may result in a less accurate recovery.

5. Microphysical Tomography

We dispose of multispectral phenomenological parameters β_Λ, $f_\Lambda(\boldsymbol{\omega}\cdot\boldsymbol{\omega}')$, g_Λ etc. Instead, we parameterize the medium by its microphysical properties, $\boldsymbol{\nu}$, which are wavelength-independent. With this parameterization, inversion scales as $\mathcal{O}(N_{\text{voxels}}N_{\text{params}})$. Direct recovery of $\boldsymbol{\nu}$ has been done in 1D plane-parallel media [40,41,43]. We focus on cases where m is known (Sec. 9 discusses a possible extension for unknown m). Tomography then seeks the size distribution parameters $\boldsymbol{\nu}(\boldsymbol{x})=[N(\boldsymbol{x}), r_{\text{e}}(\boldsymbol{x}), v_{\text{e}}(\boldsymbol{x})]$ in 3D, based on multiview projections of the scene [2].

Denote $\tilde{\boldsymbol{x}}$ as voxel *index*. The microphysical vector at this voxel is $\boldsymbol{\nu}_{\tilde{\boldsymbol{x}}}$. Define indicator functions for the voxel's spatial support $V_{\tilde{\boldsymbol{x}}}$ and solid angle $V_{\tilde{\boldsymbol{\omega}}}$ as

$$\mathbb{1}_{\tilde{\boldsymbol{x}}}(\boldsymbol{x})=\begin{cases}1 & \text{if } \boldsymbol{x}\in V_{\tilde{\boldsymbol{x}}}\\ 0 & \text{else}\end{cases}, \quad \mathbb{1}_{\tilde{\boldsymbol{\omega}}}(\boldsymbol{\omega})=\begin{cases}1 & \text{if } \boldsymbol{\omega}\in V_{\tilde{\boldsymbol{\omega}}}\\ 0 & \text{else}\end{cases}, \tag{30}$$

respectively. The continuous microphysical and radiance fields can be interpolated as[5]

$$\boldsymbol{\nu}(\boldsymbol{x}) = \sum_{\tilde{\boldsymbol{x}}} \boldsymbol{\nu}_{\tilde{\boldsymbol{x}}} \mathbb{1}_{\tilde{\boldsymbol{x}}}(\boldsymbol{x}), \tag{31}$$

$$I_\Lambda(\boldsymbol{x},\boldsymbol{\omega}) = \sum_{\tilde{\boldsymbol{x}},\tilde{\boldsymbol{\omega}}} I^\Lambda_{\tilde{\boldsymbol{x}},\tilde{\boldsymbol{\omega}}} \mathbb{1}_{\tilde{\boldsymbol{x}}}(\boldsymbol{x}) \mathbb{1}_{\tilde{\boldsymbol{\omega}}}(\boldsymbol{\omega}). \tag{32}$$

Denote $\boldsymbol{\Psi}$ and $\mathbf{I}(\boldsymbol{\Psi})$ as vectors that respectively concatenate $\boldsymbol{\nu}_{\tilde{\boldsymbol{x}}}$ and $I^\Lambda_{\tilde{\boldsymbol{x}},\tilde{\boldsymbol{\omega}}}$, across all voxels. The forward model *renders* $\mathbf{I}(\boldsymbol{\Psi})$, given $\boldsymbol{\Psi}$. Imaging is sampling of the radiance field at specific locations, directions and spectral bands. Sampling is modeled by an operator $\mathbf{M}$, resulting in a modeled vector of measurements $\mathbf{y}^{\text{model}}_{\boldsymbol{\Psi}}=\mathbf{M}\mathbf{I}(\boldsymbol{\Psi})$. On the other hand, an actual empirical system measures noisy data, denoted by $\mathbf{y}$. Using $\mathbf{y}$, the inverse problem seeks to recover an unknown medium $\boldsymbol{\Psi}$. Generally, the solution minimizes a cost function

$$\hat{\boldsymbol{\Psi}} = \arg\min_{\boldsymbol{\Psi}} [\mathcal{D}(\mathbf{y}, \mathbf{y}^{\text{model}}_{\boldsymbol{\Psi}}) + \mathcal{R}(\boldsymbol{\Psi})], \tag{33}$$

where $\mathcal{R}$ is a regularization term that expresses prior knowledge about $\boldsymbol{\Psi}$, while $\mathcal{D}$ is a data (fidelity) term. The particular choice of $\mathcal{R}$ and $\mathcal{D}$ functionals affects the solution and the minimization speed. Nevertheless, the core ability to recover $\boldsymbol{\Psi}$ depends on the forward model.

The field $\boldsymbol{\Psi}$ has continuous-valued variables. Moreover, rendering $\mathbf{y}^{\text{model}}_{\boldsymbol{\Psi}}$ depends continuously and smoothly on $\boldsymbol{\Psi}$. Hence, for efficient minimization, the *gradient* with respect to $\boldsymbol{\Psi}$ can be exploited. An easily differentiable term is

$$\mathcal{D}(\mathbf{y}, \mathbf{y}^{\text{model}}_{\boldsymbol{\Psi}}) = \|\mathbf{y} - \mathbf{M}\mathbf{I}(\boldsymbol{\Psi})\|_2^2. \tag{34}$$

[5] Often, more elaborate interpolation schemes are employed [14].

Then,

$$\frac{\partial \mathcal{D}}{\partial \boldsymbol{\Psi}} = 2\left[\mathbf{M}\mathbf{I}(\boldsymbol{\Psi}) - \mathbf{y}\right]^\top \mathbf{M} \frac{\partial \mathbf{I}(\boldsymbol{\Psi})}{\partial \boldsymbol{\Psi}}. \tag{35}$$

Here $(\cdot)^\top$ denotes transposition. The gradient (35) can enable an efficient solution to Eq. (33).

6. Functional Gradients

We express the functional gradients directly on the microphysical properties vector $\boldsymbol{\nu}$. For a given size distribution, $n(r|\boldsymbol{\nu})$, Eqs. (22,23) are integrated, yielding an effective extinction coefficient and scattering function in a voxel

$$\beta_\Lambda(\boldsymbol{\nu}) = \beta^{\text{Rayl}}_\Lambda + \int n(r|\boldsymbol{\nu}) \sigma^{\text{Mie}}_\Lambda(r|m) \mathrm{d}r, \tag{36}$$

$$f_\Lambda(\mu|\boldsymbol{\nu}) = f^{\text{Rayl}}_\Lambda(\mu) + \int n(r|\boldsymbol{\nu}) f^{\text{Mie}}_\Lambda(\mu, r|m) \mathrm{d}r. \tag{37}$$

In the atmosphere, with localized tornadoes as exception, $\sigma^{\text{Rayl}}_\lambda$ and N^{Rayl} due to air molecules vary slowly in space and time. They are mapped over Earth using long established systems and are mainly a function of altitude. Three-dimensional variations to derive are therefore attributed to variations in $\boldsymbol{\nu}$. The gradients of (36,37) with respect to $\boldsymbol{\nu}$ are thus

$$\frac{\partial}{\partial \boldsymbol{\nu}} \beta_\Lambda(\boldsymbol{\nu}) = \int \frac{\partial n(r|\boldsymbol{\nu})}{\partial \boldsymbol{\nu}} \sigma^{\text{Mie}}_\Lambda(r|m) \mathrm{d}r, \tag{38}$$

$$\frac{\partial}{\partial \boldsymbol{\nu}} f_\Lambda(\mu|\boldsymbol{\nu}) = \int \frac{\partial n(r|\boldsymbol{\nu})}{\partial \boldsymbol{\nu}} f^{\text{Mie}}_\Lambda(\mu, r|m) \mathrm{d}r. \tag{39}$$

For a *Gamma*-distribution (3), the derivatives with respect to parameters (1,2) are:

$$\frac{\partial n(r|\boldsymbol{\nu})}{\partial N} = C r^{(v_{\text{e}}^{-1}-3)} \exp\left(-\frac{r}{r_{\text{e}} v_{\text{e}}}\right), \tag{40}$$

$$\frac{\partial n(r|\boldsymbol{\nu})}{\partial r_{\text{e}}} = \frac{r + 2 r_{\text{e}} v_{\text{e}} - r_{\text{e}}}{r_{\text{e}}^2 v_{\text{e}}} n(r|\boldsymbol{\nu}), \tag{41}$$

$$\frac{\partial n(r|\boldsymbol{\nu})}{\partial v_{\text{e}}} = \frac{\psi(\frac{1}{v_{\text{e}}} - 2) - \log\frac{r}{r_{\text{e}} v_{\text{e}}} - 1 + 2v_{\text{e}} + r r_{\text{e}}^{-1}}{v_{\text{e}}^2} n(r|\boldsymbol{\nu}). \tag{42}$$

Here $\psi = \mathrm{d}\log\Gamma(x)/\mathrm{d}x$ is the *digamma* function. Equations (40,41,42) are used to compute the integrals of (38,39). We incorporate these functional gradients (Eqs. 38,39) into the radiative transfer equations as follows. Define

$$\frac{\partial}{\partial \boldsymbol{\nu}_{\tilde{\boldsymbol{x}}}} T_\Lambda(\boldsymbol{x}_1, \boldsymbol{x}_2) = -T_\Lambda(\boldsymbol{x}_1, \boldsymbol{x}_2) \int_{\boldsymbol{x}_1}^{\boldsymbol{x}_2} \frac{\partial \beta_\Lambda(\boldsymbol{\nu})}{\partial \boldsymbol{\nu}_{\tilde{\boldsymbol{x}}}} \mathbb{1}_{\tilde{\boldsymbol{x}}}(\boldsymbol{s}) \mathrm{d}\boldsymbol{s}. \tag{43}$$

Then, using (27,28), the coupled equations describing the radiance approximate gradient with respect to $\boldsymbol{\nu}$ are

$$\frac{\partial}{\partial \boldsymbol{\nu}_{\tilde{\boldsymbol{x}}}} \bar{I}_\Lambda(\boldsymbol{x}, \boldsymbol{\omega}) = I^{\text{BC}}_\Lambda(\boldsymbol{x}_0, \boldsymbol{\omega}) \frac{\partial}{\partial \boldsymbol{\nu}_{\tilde{\boldsymbol{x}}}} T_\Lambda(\boldsymbol{x}, \boldsymbol{x}_0) + \int_{\boldsymbol{x}}^{\boldsymbol{x}_0} \left[\frac{\partial \bar{J}_\Lambda(\boldsymbol{x}', \boldsymbol{\omega})}{\partial \boldsymbol{\nu}_{\tilde{\boldsymbol{x}}}} T_\Lambda(\boldsymbol{x}, \boldsymbol{x}') + \bar{J}_\Lambda(\boldsymbol{x}', \boldsymbol{\omega}) \frac{\partial T_\Lambda(\boldsymbol{x}, \boldsymbol{x}')}{\partial \boldsymbol{\nu}_{\tilde{\boldsymbol{x}}}}\right] \mathrm{d}\boldsymbol{x}' \tag{44}$$

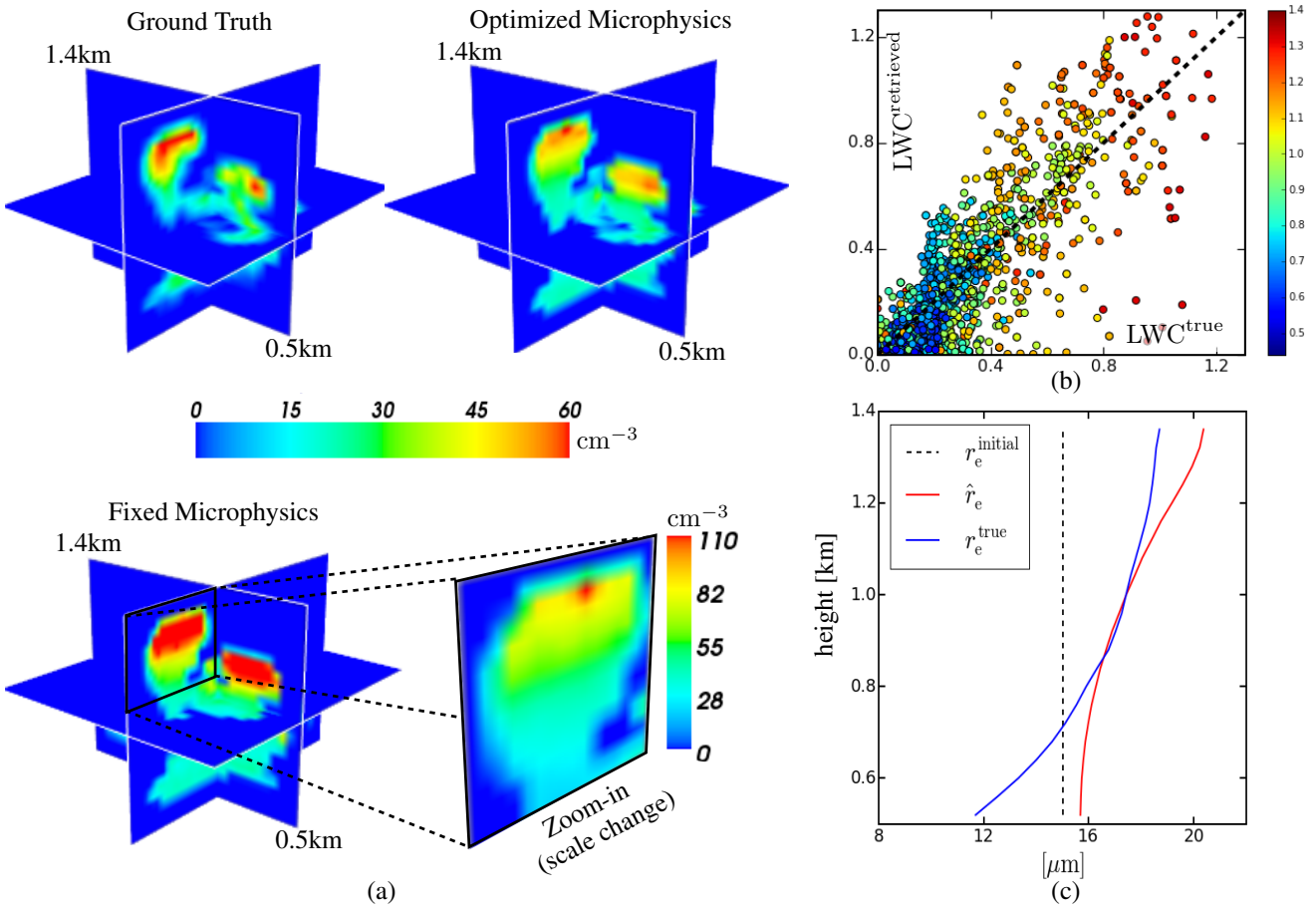

Figure 6. Recovery of *microphysical* parameters $\boldsymbol{\nu} = \{N, r_{\text{e}}, v_{\text{e}}\}$. (a) Recovery of total number density, N, in 3D. [Bottom] Prior approach [35], assumes fixed microphysics, resulting in a recovery bias towards more droplets, due to a fixed smaller effective radius. (b) Scatter plot of the recovered $\mathbb{M}_{\text{w}}$. Color corresponds to altitude [km]. (c) Recovery of r_{e} as a function of altitude.

$$\frac{\partial}{\partial \boldsymbol{\nu}_{\tilde{\boldsymbol{x}}}} \bar{J}_{\Lambda}\left(\boldsymbol{x}, \boldsymbol{\omega}\right) = \int_{4\pi} \bar{I}_{\Lambda}(\boldsymbol{x}, \boldsymbol{\omega}') \frac{\partial f_{\Lambda}(\boldsymbol{\omega}\cdot\boldsymbol{\omega}'|\boldsymbol{\nu})}{\partial \boldsymbol{\nu}_{\tilde{\boldsymbol{x}}}} \mathbb{1}_{\tilde{\boldsymbol{x}}}(\boldsymbol{x}) \mathrm{d}\boldsymbol{\omega}' + \int_{4\pi} \frac{\partial \bar{I}_{\Lambda}(\boldsymbol{x}, \boldsymbol{\omega})}{\partial \boldsymbol{\nu}_{\tilde{\boldsymbol{x}}}} f_{\Lambda}(\boldsymbol{x}, \boldsymbol{\omega}\cdot\boldsymbol{\omega}') \mathrm{d}\boldsymbol{\omega}'. \tag{45}$$

The coupling of Eqs. (44,45) makes the gradient computation highly complex, requiring recursion. Starting with an initial guess of $\boldsymbol{\nu}^{\text{initial}}$, a gradient-based update (Eq. 35) is computed using an approximation that builds upon Eqs. (44,45). The basic principle of the approximation ignores the second integral term in the gradient of J (Eq. 45). This decouples the gradient of I from the gradient of J in the recursion of (44,45). See Ref. [35] for more information about this approximation. This constitutes an iterative algorithm for solving (33).

7. Numerical Simulation

The derived mathematical model and algorithm principles can be applied to various scattering media. We use liquid water clouds as a case-study, recovering the droplet size distribution parameters (Eqs. 1,2). We simulate an atmosphere with molecular Rayleigh scattering and a liquid water cloud. For realistic complexity, an LES [10,37] generates a cloud field. In this field, N varies on a 3D grid, r_{e} varies only with altitude [28], while $v_{\text{e}}^{\text{true}}$=0.1 is constant within the cloud (Fig. 6). $\mathcal{R}$=$0.1\|\partial_z r_{\text{e}}\|^2$. For computational speed we pre-compute (37,36,38,39) for $r_{\text{e}} \in [1, 25]\,\mu\text{m}$ and $v_{\text{e}} \in [0.05, 0.4]$ with steps of $\Delta r_{\text{e}} \simeq 0.25\,\mu\text{m}$ and $\Delta v_{\text{e}} \simeq 0.003$.

For Mie computations (16,17) and microphysical integration (36,37), we rely on the publicly available code of [15], which had been validated rigorously.[6] A spherical harmonic discrete ordinate method (SHDOM) code [14] renders measurements similar to those taken by the AirMSPI at 20m resolution [13]. The nine viewing zenith angles are $\pm 70.5°$, $\pm 60°$, $\pm 45.6°$, $\pm 26.1°$, and $0°$, where $\pm$ indicates forward/backward along a north-bound flight path. Photon, quantization and dark noise are added according to

[6] https://i3rc.gsfc.nasa.gov/

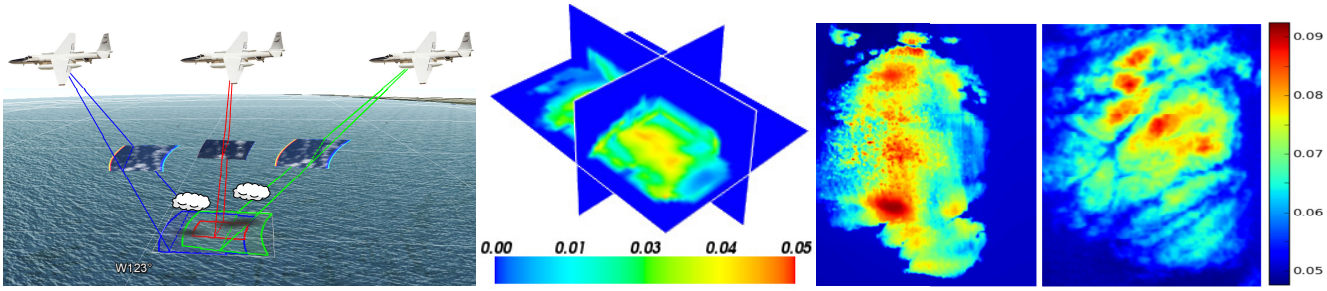

Figure 7. (a) AirMSPI sensor onboard NASA's high altitude ER-2 aircraft, acquiring multiple views of a domain over the Pacific ocean [35]. (b) Volumetric recovery using real AirMSPI data. (c) Novel view point and wavelength rendering. (d) Corresponding AirMSPI acquired image. Artifacts evident in the rendered view are partially due to errors in the rigid-body registration of the cloud movement.

AirMSPI parameters. The spectral bands Λ considered here are those of AirMSPI.

We analyze an atmospheric volume with dimensions of $0.64\times0.72\times20\,\mathrm{km}^3$ with cloud voxel size of $20\times20\times40\,\mathrm{m}^3$. Pre-processing by space-carving [50] reduces the cloud domain that we seek to recover. For initialization, we used constant values

$$N^{\mathrm{initial}}=0\,\mathrm{cm}^{-3},\ r_{\mathrm{e}}^{\mathrm{initial}}=15\,\mu\mathrm{m},\ v_{\mathrm{e}}^{\mathrm{initial}}=0.4. \tag{46}$$

Convergence takes 100 iterations. The estimated effective variance is $\hat{v}_{\mathrm{e}}=0.166$. Recovery results for N, r_{e}, $\mathbb{M}_{\mathrm{w}}$ (Eq. 4) are shown in Fig. 6. Results are quantitatively assessed by the retrieved $\mathbb{M}_{\mathrm{w}}$ at every voxel. The relative average error and total mass errors [2] are respectively

$$\epsilon=\frac{\|\mathbb{M}_{\mathrm{w}}^{\mathrm{true}}-\mathbb{M}_{\mathrm{w}}^{\mathrm{retrieved}}\|_1}{\|\mathbb{M}_{\mathrm{w}}^{\mathrm{true}}\|_1},\ \delta=\frac{\|\mathbb{M}_{\mathrm{w}}^{\mathrm{true}}\|_1-\|\mathbb{M}_{\mathrm{w}}^{\mathrm{retrieved}}\|_1}{\|\mathbb{M}_{\mathrm{w}}^{\mathrm{true}}\|_1}. \tag{47}$$

The extinction $\beta_\Lambda(\boldsymbol{x})$ is transformed into $N(\boldsymbol{x})$ using (3,36)

$$\hat{N}=\frac{\hat{\beta}_\Lambda-\beta_\Lambda^{\mathrm{Rayl}}}{\int\hat{C}r^{(\hat{v}_{\mathrm{e}}^{-1}-3)}\exp\left(-\frac{r}{\hat{r}_{\mathrm{e}}\hat{v}_{\mathrm{e}}}\right)\sigma_\Lambda^{\mathrm{Mie}}(r|m)\mathrm{d}r}. \tag{48}$$

Using (48), our method can be compared to a prior approach [35], which estimates $\beta_\Lambda(\boldsymbol{x})$, assuming fixed microphysics (46). For fixed $r_{\mathrm{e}}^{\mathrm{initial}}$, $v_{\mathrm{e}}^{\mathrm{initial}}$ (Eq. 46), method [35] yields $\epsilon=48\%, \delta=-55\%$. Leveraging our full microphysical optimization reduces the errors to $\epsilon=40\%$ and $\delta=-8\%$. A spatial distribution of the recovered parameters is given in Fig. 6.

8. Real-World Data: AirMSPI

We apply this approach to real measurements, captured outdoors from multiple remote views at several bands, using AirMSPI [13]. AirMSPI signals had undergone extensive geometric and radiometric calibration, thus enabling highly accurate quantitative measurements [13].

Pre-processing: Clouds are segmented from the ocean (Fig. 9). Non cloudy pixels are used to estimate the ocean albedo per Λ. Cloudy pixels were used to estimate the cloud velocity, $\sim11\,\mathrm{m/s}$, and register the images (see Appendix).

3D recovery: A voxel resolution of $20\times20\times20\,\mathrm{m}^3$is used. Tomography is preformed using six of the eight spectral bands of AirMSPI (Fig. 7). The estimated cloud water mass is $\sim1070\,\mathrm{kg}$. To assess the recovery, we render the cloud at an unused band, $380\pm16\,\mathrm{nm}$.

9. Discussion

This work derives a mathematical framework for 3D tomography of scatterer microphysics. It uses multispectral multi-view 3D data. We believe this principle can impact various fields, including atmospheric science. The approach can be applied beyond remote sensing, in fields such as computer graphics and bio-medical imaging, where the model holds. This includes tissue, where incoherent scattering applies [25].

The non-convexity of the forward model makes gradient-based optimization (33-35) dependent on initial conditions. Thus, recovery can be improved using more sophisticated initializations and algorithms. Furthermore, recovery error tends to grow with optical depth. This insight can lead to a tailored regularization scheme.

The recovery error depends on the view and illumination angles. For a fixed $v_{\mathrm{e}}=0.1$, we quantify angular and spectral sensitivities of $r_{\mathrm{e}}\in\left[r_{\mathrm{e}}^{\min},r_{\mathrm{e}}^{\max}\right]=[5,25]\,\mu\mathrm{m}$

$$\chi_{r_{\mathrm{e}}}(\theta,\Lambda)=\int_{r_{\mathrm{e}}^{\min}}^{r_{\mathrm{e}}^{\max}}\left|\frac{\partial f_\Lambda(\mu|\boldsymbol{\nu})}{\partial r_{\mathrm{e}}}\right|\mathrm{d}r_{\mathrm{e}}. \tag{49}$$

Figure 8 indicates high sensitivity in the forward peak (0°), rainbow and glory angles $(140^\circ,180^\circ)$ and circa 120° in the UV. Forward peak sensitivity implies that incorporating ground measurements [2,26,27,50] is informative for effective radius recovery.

In applications where the scattering particles' material is unknown, an optimization procedure for m is required. The sought microphysical parameter vector is then generalized

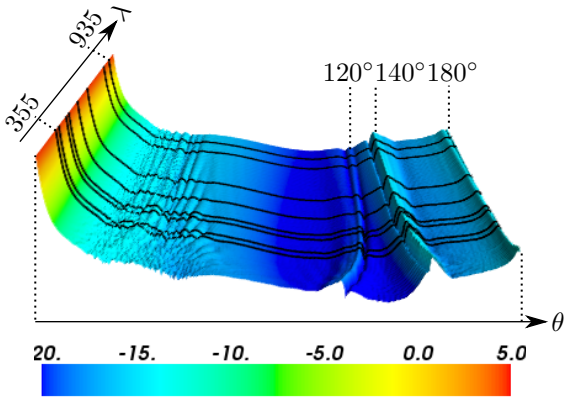

Figure 8. Spectral-angular sensitivity, $\log[\chi_{r_e}(\theta,\Lambda)]$. Black stripes indicate Airborne Multiangle SpectroPolarimetric Imager (AirMSPI) spectral bands [13].

to $\boldsymbol{\nu}=[N, r_e, v_e, m]$ per $\boldsymbol{x}$. Equations (38,39) become

$$\frac{\partial}{\partial \boldsymbol{\nu}}\beta_\Lambda(\boldsymbol{\nu}) = \int \frac{\partial n}{\partial \boldsymbol{\nu}}\sigma_\Lambda^{\text{Mie}}\mathrm{d}r + \int n\frac{\partial \sigma_\Lambda^{\text{Mie}}}{\partial \boldsymbol{\nu}}\mathrm{d}r, \tag{50}$$

$$\frac{\partial}{\partial \boldsymbol{\nu}}f_\Lambda(\mu|\boldsymbol{\nu}) = \int \frac{\partial n}{\partial \boldsymbol{\nu}}f_\Lambda^{\text{Mie}}\mathrm{d}r + \int n\frac{\partial f_\Lambda^{\text{Mie}}}{\partial \boldsymbol{\nu}}\mathrm{d}r. \tag{51}$$

The dependency of (16,17,22,23) on $\boldsymbol{\nu}$ is only through m

$$\frac{\partial}{\partial m}\sigma_\Lambda^{\text{Mie}}(r|m)=\frac{1}{B_\Lambda^{\text{tot}}}\int_{\lambda\in\Lambda}B(\lambda)\frac{\partial}{\partial m}\sigma_\lambda^{\text{Mie}}(r|m)\mathrm{d}\lambda, \tag{52}$$

$$\frac{\partial}{\partial m}f_\Lambda^{\text{Mie}}(\mu,r|m)=\frac{1}{B_\Lambda^{\text{tot}}}\int_{\lambda\in\Lambda}B(\lambda)\frac{\partial}{\partial m}f_\lambda^{\text{Mie}}(\mu,r|m)\mathrm{d}\lambda, \tag{53}$$

where

$$\frac{\partial}{\partial m}\sigma_\lambda^{\text{Mie}}(r|m)=\frac{\lambda^2}{2\pi}\sum_{l=1}^{\infty}(2l+1)\Re\left(\frac{\partial a_l^\lambda}{\partial m}+\frac{\partial b_l^\lambda}{\partial m}\right), \tag{54}$$

$$\frac{\partial}{\partial m}f_\lambda^{\text{Mie}}(\mu,r|m)=\frac{\lambda^2}{8\pi^2}\left(\frac{\partial|S_1^\lambda|^2}{\partial m}+\frac{\partial|S_2^\lambda|^2}{\partial m}\right). \tag{55}$$

The derivative of the modulus squared (Eq. 55) is given by

$$\frac{\partial|S_\star^\lambda|^2}{\partial m}=2\left[\Re(S_\star^\lambda)\Re\left(\frac{\partial S_\star^\lambda}{\partial m}\right)+\Im(S_\star^\lambda)\Im\left(\frac{\partial S_\star^\lambda}{\partial m}\right)\right], \tag{56}$$

where $\star=1,2$ and $\Im$ denotes the imaginary part. The dependency of (14,15) on m is through the coefficients (11,12). Derivatives are thus computed by linearly superposing the derivatives of (11,12):

$$\frac{\partial a_l^\lambda(r|m)}{\partial m}=\frac{z\Psi_l(z)\Psi_l''(z)-z\Psi_l'^2(z)-\Psi_l(z)\Psi_l'(z)}{-i\left[\xi_l(d)\Psi_l'(z)-m\xi_l'(d)\Psi_l(z)\right]^2} \tag{57}$$

$$\frac{\partial b_l^\lambda(r|m)}{\partial m}=\frac{z\Psi_l(z)\Psi_l''(z)-z\Psi_l'^2(z)+\Psi_l(z)\Psi_l'(z)}{-i\left[\xi_l(d)\Psi_l'(z)-m\xi_l'(d)\Psi_l(z)\right]^2} \tag{58}$$

where $z=md$. See Ref. [20] for complete derivations of Mie derivatives and stable computation procedures.

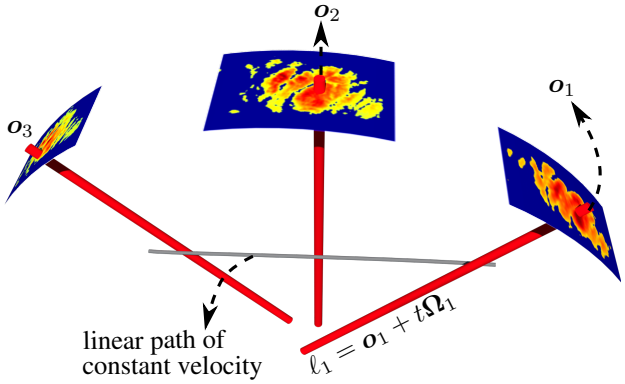

Figure 9. 3D registration process. A path of constant velocity minimizes the distance from COM lines $\{\ell_k\}_{k=1}^{N_{\text{views}}}$.

Appendix : Registration

We describe the registration process used in Sec. 8. Denote the number of views by N_{views}. Let $\{\boldsymbol{o}\}_{k=1}^{N_{\text{views}}}$ denote cloud radiance center of mass (COM) coordinates in each image. Each image COM corresponds to a particular ray in 3D, with direction vector $\boldsymbol{\Omega}_k$. Points on the COM ray (Fig. 9) are thus

$$\ell_k = \{\boldsymbol{o}_k + t\boldsymbol{\Omega}_k \quad -\infty < t < \infty\} \tag{59}$$

Define a point-to-line distance as

$$D(\ell_k, \boldsymbol{x}) = \|\boldsymbol{o}_k - \boldsymbol{x} - [(\boldsymbol{o}_k - \boldsymbol{x})\cdot\boldsymbol{\Omega}_k]\boldsymbol{\Omega}_k\|^2 \tag{60}$$

To estimate a constant velocity $\boldsymbol{v}$ of a cloud, one view serves as a reference frame denoted by $k=0$. The cloud's apparent 3D COM is $\boldsymbol{x}_{\text{COM}}$. Let Δ_k be the time difference between frame k and the reference frame, for which $\Delta_0=0$. We estimate the 3D path of a moving COM by

$$\{\hat{\boldsymbol{x}}_{\text{COM}}, \hat{\boldsymbol{v}}\} = \arg\min_{\boldsymbol{x},\boldsymbol{v}} \sum_{k=1}^{N_{\text{views}}} D(\ell_k, \boldsymbol{x}+\Delta_k\boldsymbol{v}). \tag{61}$$

To enable tomographic reconstruction, we register each measured image to the moving reference frame $\{\hat{\boldsymbol{x}}_{\text{COM}}+\Delta_k\hat{\boldsymbol{v}}\}$.

Acknowledgments: We thank A. Aides, M. Sheinin, D. Diner and D. Rosenfeld for fruitful discussions. We thank G. Matheou, Z. Qu, I. Talmon and AWS Cloud Credits for technical support. The authors are grateful to the US-Israel Binational Science Foundation (BSF), for continuously facilitating our international collaboration by a joint grant. AD's work was carried out at JPL, California Inst. of Tech., supported by NASA's SMD/ESD/RST and ESTO/AIST programs. YYS is a Landau Fellow - supported by the Taub Foundation and Israeli Ministry of Science, Technology and Space (Grant 3-13602). His work is conducted in the Ollendorff Minerva Center (BMBF).

References

[1] M. Abramowitz, and I. A. Stegun. *Handbook of mathematical functions: with formulas, graphs, and mathematical tables,* Courier Corp., 1964.

[2] A. Aides, Y. Y. Schechner, V. Holodovsky, M. J. Garay, and A. B. Davis. "Multi sky-view 3D aerosol distribution recovery," Opt. Express, 21:25820–25833, 2013.

[3] D. Akkaynak, T. Treibitz, T. Shlesinger, R. Tamir, Y. Loya, and D. Iluz. "What is the space of attenuation coefficients in underwater computer vision?," Proc. IEEE CVPR, 2017.

[4] B. Atcheson, I. Ihrke, W. Heidrich, A. Tevs, D. Bradley, M. Magnor, and H.-P. Seidel. "Time-resolved 3D capture of non-stationary gas flows," Proc. ACM TOG, 27:132, 2008.

[5] D. Berman, T. Treibitz, and S. Avidan "Air-light estimation using haze-lines," Proc. IEEE ICCP, 2017.

[6] D. A. Boas, D. H. Brooks, E. L. Miller, C. A. DiMarzio, M. Kilmer, R. J. Gaudette, and Q. Zg. "Imaging the body with diffuse optical tomography," IEEE Signal Proc. Mag., 18(6):57–75, 2001.

[7] C. F. Bohren, and D. R. Huffman. "Absorption and scattering of light by small particles," John Wiley & Sons, 2008.

[8] S. Chandrasekhar. *Radiative Transfer,* Dover Pub., 1960.

[9] Y.-C. Chen, M. W. Christensen, G. L. Stephens, and J. H. Seinfeld. "Satellite-based estimate of global aerosol-cloud radiative forcing by marine warm clouds," Nature Geo., 2014.

[10] D. Chung and G. Matheou. "Large-eddy simulation of stratified turbulence. Part I: A vortex-based subgrid-scale model," J. Atmos. Sci., 71:1863–1879, 2014.

[11] A. B. Davis and A. Marshak. "Solar radiation transport in the cloudy atmosphere: A 3D perspective on observations and climate impacts," Rep. Prog. Phys., 73:026801, 2010.

[12] D. J. Diner and J. V. Martonchik, "Atmospheric transmittance from spacecraft using multiple view angle imagery," App. Opt., 25:3503-3511, 1985.

[13] D. J. Diner, F. Xu, M. J. Garay, J. V. Martonk, B. Rheingans, S. Geier, Ab. Davis, B. Hancock, V. Jovanovic, and M. Bull. "The Airborne Multiangle SpectroPolarimetric Imager (AirMSPI): A new tool for aerosol and cloud remote sensing," Atmos. Meas. Tech., 6:2007–2025, 2013.

[14] K. F. Evans. "The spherical harmonics discrete ordinate method for three-dimensional atmospheric radiative transfer," J. Atmos. Sci., 55:429–446, 1998.

[15] K. F. Evans. nit.colorado.edu

[16] I. Gkioulekas, B. Xiao, S. Zhao, E. H. Adelson, T. Zickler, and K. Bala. "Understanding the role of phase function in translucent appearance," Proc. ACM TOG, 32(5):147, 2013

[17] I. Gkioulekas, S. Zhao, K. Bala, T. Zickler, and A. Levin. "Inverse volume rendering with material dictionaries," Proc. ACM TOG, 32:162, 2013.

[18] I. Gkioulekas, A. Levin and T. Zickler. "An evaluation of computational imaging techniques for heterogeneous inverse scattering," Proc. ECCV, 685-701, 2016.

[19] M. E. Gorbunov, S. V. Sokolovsky, L. Bengtsson "Space refractive tomography of the atmosphere: modeling of direct and inverse problems," Max-Planck Inst. fur Meteorologie, Report 210, 1996.

[20] R. G. Grainger, J. Lucas, G. E. Thomas and G. B. Ewen. "Calculation of Mie derivatives," Applied Optics, 43:5386-5393, 2004.

[21] J. Gregson, M. Krimerman, M. B. Hullin and W. Heidrich "Stochastic tomography and its applications in 3D imaging of mixing fluids," SIGGRAPH 2012.

[22] J. E. Hansen and L. D. Travis. "Light scattering in planetary atmospheres," Space Science Rev. 16:527-610, 1974.

[23] J. E. Hansen. "Multiple scattering of polarized light in planetary atmospheres, Part II. Sunlight reflected by terrestrial water clouds," J. of Atmos. Sci, 28(8): 1400-1426, 1971.

[24] L. G. Henyey, and J. L. Greenstein. "Diffuse radiation in the galaxy," The Astrophysical Journal 93: 70-83, 1941.

[25] R. Hochuli, S. Powell, S. Arridge, and B. Cox "Quantitative photoacoustic tomography using forward and adjoint Monte Carlo models of radiance," J. Biomed. Optics, 21(12), pp.126004-126004, 2016.

[26] B. N. Holben, T. .F. Eck, I. Slutsker, D. Tanre, J. P. Buis, A. Setzer, E. Vermote, J. A. Reagan, Y. J. Kaufman, T. Nakajima, and F. Lavenu, "AERONET - A federated instrument network and data archive for aerosol characterization," Remote sensing of environment, 66(1), pp.1-16, 1998.

[27] V. Holodovsky, Y. .Y Schechner, A. Levin, A. Levis and A. Aides. "In-situ multi-view multi-scattering stochastic tomography," Proc. IEEE ICCP, pp.1-12, 2016.

[28] W. C. Hsieh, A. Nenes, R. .C. Flagan, J. H. Seinfeld, G. Buzorius, and H. Jonsson, "Parameterization of cloud droplet size distributions: Comparison with parcel models and observations," J. of Geo. Res.: Atmos., 114(D11), 2009.

[29] Y. Ji, J. Ye, and J. Yu. "Reconstructing gas flows using light-path approximation," Proc. IEEE CVPR, 2507–2514, 2013.

[30] O. V. Kalashnikova, M. J. Garay, A. B. Davis, D. J. Diner and J. V. Martonchik "Sensitivity of multi-angle photopolarimetry to vertical layering and mixing of absorbing aerosols: Quantifying measurement uncertainties," Journal of Quantitative Spectroscopy & Radiative Transfer 112:21492163, 2011.

[31] P. Khungurn, D. Schroeder, S. Zhao, K. Bala and S. Marschner. "Matching real fabrics with micro-appearance models," ACM TOG, 35(1): 1, 2015.

[32] M. Kerker. *The Scattering of Light and Other Electromagnetic Radiation: Physical Chemistry: A Series of Monographs,* Academic press, 2013.

[33] L. Kratz and K. Nishino, "Factorizing scene albedo and depth from a single foggy image," IEEE ICCV 2009.

[34] A. A. Kokhanovsky, *Light Scattering Media Optics,* 3^{rd} edition, Springer, Berlin (2004).

[35] A. Levis, Y. Y. Schechner, A. Aides and A.B. Davis. "Airborne three-dimensional cloud tomography," Proc. IEEE ICCV, 2015.

[36] J. V. Martonchik, D. J. Diner, R. A. Kahn, T. P. Ackerman, M. M. Verstrate, B. Pinty and H. R. Gordon "Techniques for the retreival of aerosol properties over land and ocean using multiangle imaging," IEEE Trans. Geos. Rem. Sens. 36:1212-1227, 1998.

[37] G. Matheou and D. Chung. "Large-eddy simulation of stratified turbulence. Part II: Application of the stretched-vortex

model to the atmospheric boundary layer," J. Atmos. Sci., 71:4439–4460, 2014.

[38] H. Messer, A. Zinevich, and P. Alpert, "Environmental sensor networks using existing wireless communication systems for rainfall and wind velocity measurements," IEEE Instrumentation & Measurement Magazine 15/2:32-38, 2012.

[39] C. D. Mobley, *Light and water: radiative transfer in natural waters,* Academic press (1994).

[40] T. Nakajima and M. D. King. "Determination of the optical thickness and effective particle radius of clouds from reflected solar radiation measurements," Part 1: Theory. J. Atmos. Sci., 47:1878–1893, 1990.

[41] T. Nakajima, M. D. King, J. D. Spinhirne, and L. F. Radke. "Determination of the optical thickness and effective particle radius of clouds from reflected solar radiation measurements. Part 2: Marine stratocumulus observations," J. Atmos. Sci., 48(5):728–751, 1991.

[42] S. G. Narasimhan and S. K. Nayar, "Vision and the atmosphere," IJCV 48:233–254, 2002.

[43] S. Platnick, M. D. King, S. A. Ackerman, W. P. Menzel, B. A. Baum, J. C. Riédi, and R. A. Frey. "The MODIS cloud products: Algorithms and examples from Terra," IEEE T. Geosci. Remote. Sens, 41(2):459–473, 2003.

[44] R. R. Rogers and M. K. Yau. *A Short Course in Cloud Physics,* Elsevier (1996).

[45] D. Rosenfeld. "Aerosol-cloud interactions control of earth radiation and latent heat release budgets," In *Solar Variability and Planetary Climates*, pages 149–157. Springer, 2007.

[46] S. Sanghavi, J. V. Martonchik, A. B. Davis and D. J. Diner, "Linearization of a scalar Matrix Operator Method radiative transfer model with respect to aerosol and surface properties," Journal of Quantitative Spectroscopy & Radiative Transfer, 2012.

[47] Y. Y. Schechner, D. J. Diner, and J. V. Martonchik "Spaceborne underwater imaging," Proc. IEEE ICCP 2011.

[48] M. Sheinin, and Y. .Y. Schechner, "The next best underwater view," Proc. IEEE CVPR, pp. 3764-3773, 2016.

[49] O. Spier, T. Treibitz, and G. Gilboa, "In situ target-less calibration of turbid media," Proc. IEEE ICCP, 2017.

[50] D. Veikherman, A. Aides, Y. Y. Schechner, and A. Levis. "Clouds in the cloud," Proc. ACCV, 2014.

[51] T. E. Write, M. Burton, D. M. Pyle, T. Caltabiano "Scanning tomography of SO_2 distribution in a volcanic gas plume," Geophys. Res. Lett. 35:L17811, 2008.